

OX40⁺ plasmacytoid dendritic cells in the tumor microenvironment promote antitumor immunity

Kate Poropatich,^{1,2} Donye Dominguez,³ Wen-Ching Chan,⁴ Jorge Andrade,⁴ Yuanyuan Zha,⁵ Brian Wray,⁶ Jason Miska,⁷ Lei Qin,³ Lisa Cole,⁸ Sydney Coates,⁹ Urjeet Patel,^{2,9} Sandeep Samant,^{2,9} and Bin Zhang^{2,3}

¹Department of Pathology, ²Robert H. Lurie Comprehensive Cancer Center, and ³Division of Hematology/Oncology, Department of Medicine, Northwestern University Feinberg School of Medicine, Chicago, Illinois, USA. ⁴Center for Research Informatics and ⁵Human Immunologic Monitoring Facility, Office of Shared Research Facilities, University of Chicago, Chicago, Illinois, USA. ⁶Department of Biochemistry and Molecular Genetics, ⁷Department of Neurological Surgery, Northwestern University Feinberg School of Medicine, Chicago, Illinois, USA. ⁸Department of Chemistry, Northwestern University, Evanston, Illinois, USA. ⁹Head and Neck Surgery, Department of Otolaryngology, Northwestern University Feinberg School of Medicine, Chicago, Illinois, USA.

Plasmacytoid DCs (pDCs), the major producers of type I interferon, are principally recognized as key mediators of antiviral immunity. However, their role in tumor immunity is less clear. Depending on the context, pDCs can promote or suppress antitumor immune responses. In this study, we identified a naturally occurring pDC subset expressing high levels of OX40 (OX40⁺ pDC) enriched in the tumor microenvironment (TME) of head and neck squamous cell carcinoma. OX40⁺ pDCs were distinguished by a distinct immunostimulatory phenotype, cytolytic function, and ability to synergize with conventional DCs (cDCs) in generating potent tumor antigen-specific CD8⁺ T cell responses. Transcriptomically, we found that they selectively utilized EIF2 signaling and oxidative phosphorylation pathways. Moreover, depletion of pDCs in the murine OX40⁺ pDC-rich tumor model accelerated tumor growth. Collectively, we present evidence of a pDC subset in the TME that favors antitumor immunity.

Introduction

Plasmacytoid DCs (pDCs) are a pleiotropic cell population with different functions in the setting of infections, autoimmunity/inflammation, and cancer. They are perhaps best recognized for their ability to produce high levels of IFN- α through TLRs 7 and 9 in response to viruses and endogenous nucleic acids (1). In many types of human cancer, intratumoral pDCs are often tumor promoting with reduced expression of IFN- α and cell surface costimulatory molecules, and they are mediators of immunotolerance (2–11) through their expression of indoleamine 2,3-dioxygenase 1 (IDO1) and inducible T cell costimulator ligand (ICOSL) (3, 12). However, through activation of their TLRs 7 and 9, the immunostimulatory and tumor-killing functions of pDCs can be restored to enhance antitumor immunity and even drive tumor regression (13–15). In this regard, pDCs modulate immune responses that mirror their role in antiviral immunity, including enhancing the priming of cytotoxic CD8⁺ T cells by conventional DCs (cDCs) (14, 15).

In this study, we identified the accumulation of a naturally occurring immunostimulatory pDC subset in tumors and tumor-draining lymph nodes from patients with head and neck squamous cell carcinoma (HNSCC), particularly HPV-positive HNSCC, characterized by high expression of TNF receptor (TNFR) superfamily member OX40 (CD134) (OX40⁺ pDC). Like the other TNFR superfamily members, OX40 is a costimulatory

molecule expressed on activated T cells after antigenic T cell receptor (TCR) stimulation (16). The role of its expression on cells other than T lymphocytes is unclear. In pDCs, we showed that OX40⁺ pDCs were immunophenotypically and functionally distinct from their OX40-low (OX40^{lo/-} pDC) counterpart based on increased expression of cell surface maturation markers and production of IFN- α . Additionally, they synergized with autologous cDCs to generate robust tumor-associated antigen-specific (TAA-specific) CD8⁺ T cell responses. Their transcriptomes were uniquely enriched for EIF2 signaling and oxidative phosphorylation (OXPHOS) pathways. Finally, in the mouse OX40⁺ pDC-rich tumor model, they were required for limiting tumor growth. Collectively, we demonstrate OX40⁺ pDCs to be an attractive new target to boost antitumor immunity by increasing their intratumoral levels and function.

Results

OX40 expression on pDCs in the TME of HNSCC. Over a 3-year period, we performed a large prospective analysis of pDCs extracted from the tissue of patients with HNSCC ($n = 102$) (Supplemental Table 1; supplemental material available online with this article; <https://doi.org/10.1172/JCI131992DS1>). Among different myeloid and T cell immune subsets, cDCs and pDCs were major sources of OX40 expression in the TME (primary tumor and/or tumor-involved draining cervical lymph nodes [dLNs]) (Figure 1A), as measured by flow cytometry (Figure 1B) and imaged for pDCs by confocal microscopy (Figure 1C). In the TME, pDC OX40 expression was highest in the dLNs⁺, especially in patients with HPV⁺ HNSCC (Figure 1D and Supplemental Figure 1A). As ICOSL has been demonstrated to be expressed on pDCs from patients with

Conflict of interest: The authors have declared that no conflict of interest exists.

Copyright: © 2020, American Society for Clinical Investigation.

Submitted: July 22, 2019; **Accepted:** March 11, 2020; **Published:** May 26, 2020.

Reference information: *J Clin Invest*. <https://doi.org/10.1172/JCI131992>.

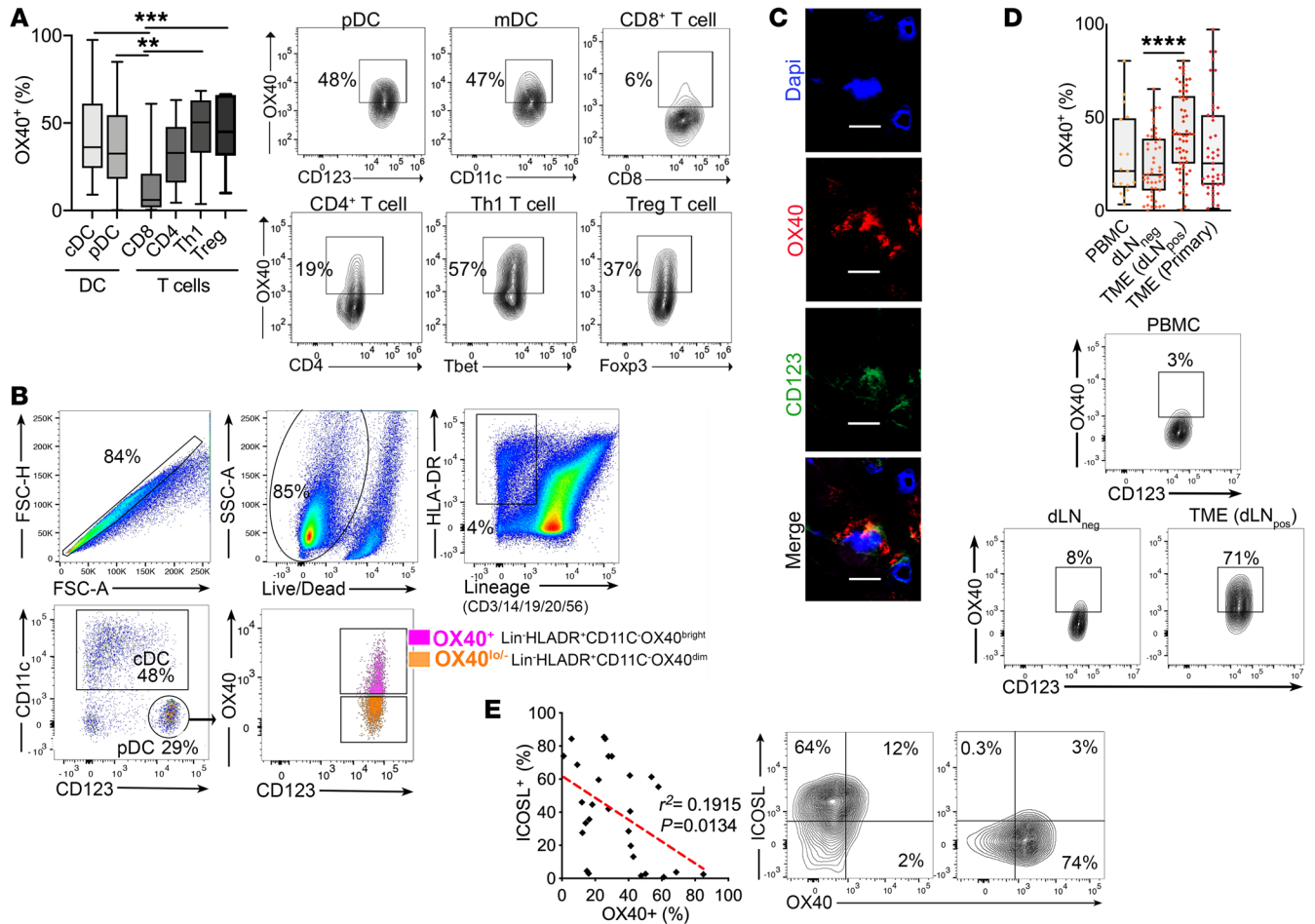


Figure 1. OX40 expression on pDCs in the TME of HNSCC. (A) OX40 expression in the TME (measured by flow cytometry) of HNSCC patients on different immune cell subsets – pDCs ($n = 89$), cDCs ($n = 53$), CD8⁺ T cells ($n = 16$), CD4⁺ T cells ($n = 17$), CD4⁺ Th1 T cells ($n = 12$), and CD4⁺ Treg cells ($n = 14$). T cell subsets were gated from live CD45⁺CD3⁺ cells. Th1 cells were defined as CD4⁺Tbet⁺ T cells and Treg cells were defined as CD4⁺Foxp3⁺ cells. **(B)** Gating strategy for FACS analysis and sorting of OX40⁺ and OX40^{lo/-} pDCs from patient specimens. After selecting for singlets and live cells, pDCs were gated from HLA-DR^{hi}Lineage⁻ cells, followed by CD11c⁺CD123⁺ cells. pDCs were further confirmed by expression of CD303 (BDCA-2). OX40 expression on pDCs was determined using internal negative controls. **(C)** Immunofluorescence of pDCs in the TME demonstrating OX40 and CD123 coexpression. $n = 4$, with 4 patient repeats. Original magnification $\times 63$. Scale bar: 5 μ m. Red, OX40; green, CD123; blue, DAPI. **(D)** OX40 expression on pDCs from different anatomic sites: PBMC ($n = 17$), dLN⁺ ($n = 50$) or dLN⁻ ($n = 59$), and primary tumor ($n = 53$). **(E)** Correlation (Pearson, with a line of best fit) between OX40 and ICOSL expression on matched patient TME pDCs ($n = 28$). One-way ANOVA followed by Tukey's post hoc test (**A** and **D**). ** $P < 0.01$; *** $P < 0.001$; **** $P < 0.0001$. Bar graph data are mean \pm SEM; middle line of box-and-whisker plot indicates the median, box limits indicate the first and third quartiles, and whiskers indicate "extreme" for all data points. Representative flow plots are shown (**A**, **D**, and **E**).

different tumors (3, 17), we examined ICOSL expression on TME pDCs and found virtually no coexpression of OX40 and ICOSL on intratumoral pDCs (Figure 1E). Our findings of increased OX40 expression on pDCs from the TME that lacked concomitant ICOSL expression led us to ask whether OX40⁺ pDCs were distinctly immunostimulatory in the TME.

OX40⁺ pDCs have a distinct immunostimulatory phenotype. We performed ex vivo characterization of FACS-isolated OX40⁺ pDCs from the dLN⁺ and tumor-negative draining cervical lymph nodes (dLN⁻) of HNSCC patients. We found that OX40⁺ pDCs represented a more mature and activated population based on increased expression of CD40, CD80, CD86, OX40L, Siglec6, and Axl (Figure 2, A and B, and Supplemental Figure 1B). OX40⁺ pDCs also had elevated expression of surface markers more commonly found on mature lymphocytes, including CD25/IL-2RA and the TNFR molecule 4-1BB.

Given the high levels of CD25 on OX40⁺ pDCs, we sought to determine whether treating pDCs with IL-2 increased their OX40 expression. We found that compared with TLR9 agonist CpG oligodeoxynucleotides (CpG ODN) and TLR 7/8 agonist Resiquimod, overnight treatment of pDCs from the dLN⁻ of HNSCC patients with IL-2 resulted in greater mean pDC OX40 expression (Supplemental Figure 1C). Stimulation of OX40⁺ pDCs with Resiquimod yielded greater percentages of IL-12p70 and CD86 coexpression compared with autologous OX40^{lo/-} pDCs and cDCs (Figure 2C). Similarly, compared with OX40^{lo/-} pDCs, stimulation of OX40⁺ pDCs with either Resiquimod or CpG resulted in elevated levels of TNF-related apoptosis-inducing ligand (TRAIL), granzyme B (GzB), and IFN- α (Figure 2, D and E) that corresponded morphologically with increased cytoplasmic secretory granularity (Figure 2F).

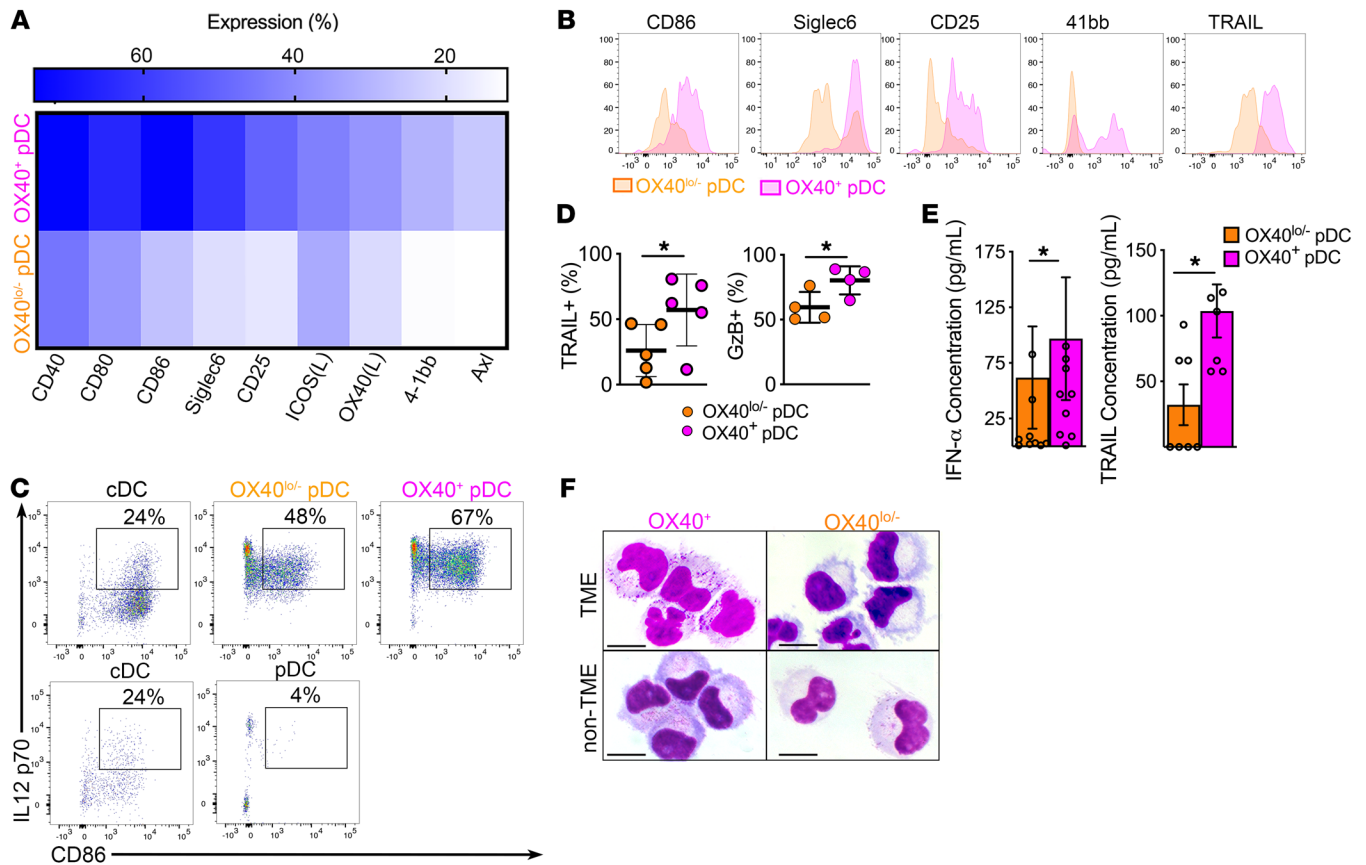


Figure 2. OX40⁺ pDCs have a distinct immunostimulatory phenotype. (A) After overnight incubation, pDCs from the dLNs of HNSCC patients ($n = 7$) were harvested and measured by flow cytometry for expression of different surface markers. Single gradient mean values are shown. (B) Representative histograms of OX40⁺ and OX40^{lo/-} pDC surface marker expression. (C) Expression of IL-12p70⁺CD86⁺ populations on sorted cDCs and pDCs, either unstimulated (controls; bottom) or in the presence of Resiquimod (top). $n = 2$; 2 experimental patient repeats. (D) Percentages (by flow cytometry) of dLN⁺ pDCs positive for TRAIL ($n = 5$) and GzB ($n = 4$) after overnight stimulation with CpG or Resiquimod. (E) The concentration (pg/mL) of IFN- α ($n = 10$) and TRAIL ($n = 6$) in the supernatant from sorted OX40⁺ and OX40^{lo/-} pDCs from the TME and non-TME stimulated with either CpG or Resiquimod. Data normalized to 2×10^3 pDCs per sample. (F) May-Grunwald staining of OX40⁺ and OX40^{lo/-} pDC subsets stimulated with Resiquimod. Scale bar: 5 μm . $n = 4$, 4 experimental patient repeats. Two-way ANOVA with Sidak's test for multiple comparisons (A). Two-tailed paired t test (D and E). * $P < 0.05$. Bar graph data are mean \pm SEM; middle line of box-and-whisker plot indicates the median, box limits indicate the first and third quartiles, and whiskers indicate "extreme" for all data points.

Collectively, our data demonstrate that OX40⁺ pDCs have a distinct expression profile of both myeloid and lymphocytic activation and maturation markers as well as selective enhanced sensitivity to TLR agonists.

OX40⁺ pDCs promote antigen-specific CD8⁺ T cell responses. Identifying OX40⁺ pDC as a mature and immunostimulatory pDC population, we hypothesized that they positively contributed to the generation of antigen-specific CD8⁺ T cell responses. As it has been shown that pDCs are capable of enhancing cDC cross-priming of CD8⁺ T cells to drive antitumor responses (14, 18), we postulated that OX40⁺ pDCs preferentially synergize with cDCs to enhance their presentation of TAA to autologous CD8⁺ T cells. We cocultured HNSCC patient pDC subsets sorted from tumors or dLNs with autologous CD8⁺ T cells and TAA-loaded autologous HLA-A2⁺ monocyte-derived DCs (mDCs) (Methods, Figure 3A, and Supplemental Figure 1D). We found that OX40⁺ pDCs, especially those from the TME, were superior to both OX40^{lo/-} pDCs and peptide-loaded mDC-only controls in boosting mDC priming of TAA-specific CD8⁺ T cells based on increased CD8⁺ T cell proliferation, expression of Tbet, and production of IFN- γ and GzB (Figure 3, B–E, and Supplemental Figure 1, E–G).

We next sought to determine whether this synergy between OX40⁺ pDCs with mDCs and CD8⁺ T cells was contact dependent or the result of secreted immunostimulatory cytokines. Using a Transwell coculture assay (Figure 3F), we found that separation of OX40⁺ but not OX40^{lo/-} pDCs from autologous peptide-loaded mDCs and CD8⁺ T cells significantly reduced CD8⁺ T cell proliferation and cytolytic function (Figure 3G). Separation of either OX40⁺ or OX40^{lo/-} pDCs from mDCs and CD8⁺ T cells resulted in reduced CD8⁺ T cell activation (Supplemental Figure 2A).

These findings suggest that OX40⁺ pDCs interact with both cDCs and CD8⁺ T cells in a distinct contact-based fashion to enhance the generation of antigen-specific effector CD8⁺ T cells. To determine whether this contact was in part based on the direct presentation of antigen by pDCs to CD8⁺ T cells, we compared the TAA-presentation capacities of OX40⁺ and OX40^{lo/-} pDCs to mDCs from HLA-A2⁺ HNSCC patients. We found when loaded with E7, OX40⁺ pDCs yielded higher percentages of antigen-specific IFN- γ - and GzB-producing CD8⁺ T cells compared with autologous OX40^{lo/-} pDCs and mDCs

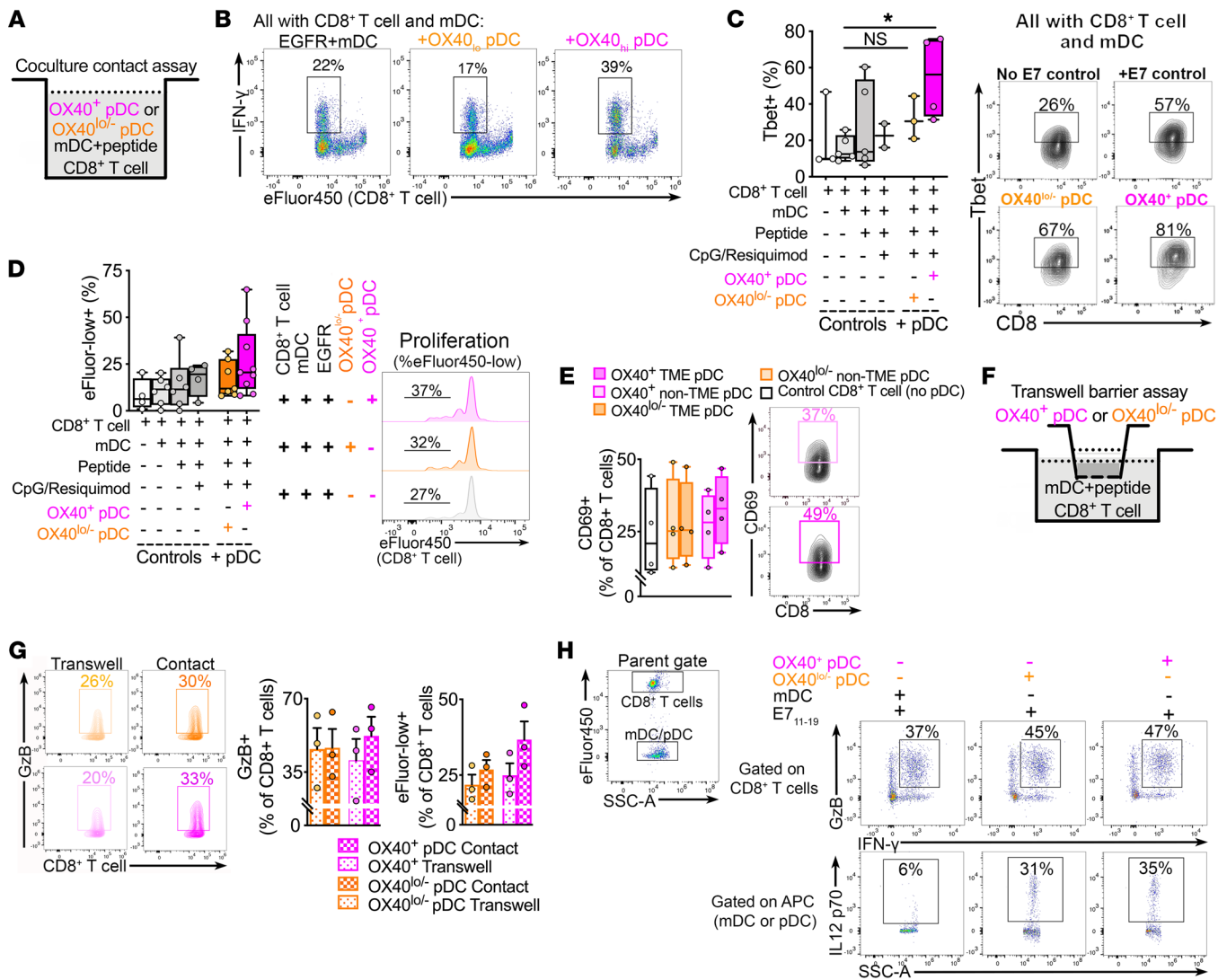


Figure 3. OX40⁺ pDCs promote antigen-specific CD8⁺ T cell responses. (A) Illustration of the antigen-specific in vitro coculture model, in which autologous OX40⁺/OX40^{lo/-} pDCs from the TME/non-TME of HNSCC patients (*n* = 9) were cocultured with autologous TAA peptide-loaded mDCs and CD8⁺ T cells for 5 to 6 days, at which point antigen-specific CD8⁺ T cell responses were measured, (B) including for proliferation (eFluor 450-low) and IFN- γ production as demonstrated in flow plots of a patient's CD8⁺ T cells cocultured with OX40⁺ or OX40^{lo/-} pDCs sorted from their tumors. CD8⁺ T cell positivity was also measured for (C) Tbet and (D) eFluor 450-low in these coculture experiments. (E) CD8⁺ T cell positivity for CD69 after coculture with TAA peptide-loaded mDCs without pDCs (control) or with OX40⁺ or OX40^{lo/-} pDCs from the TME versus non-TME (dLN⁻) (*n* = 5). (F) Illustration depicting the Transwell coculture assay in which OX40⁺ or OX40^{lo/-} pDCs in the top chamber were separated from autologous CD8⁺ T cells and peptide-loaded mDCs in the bottom chamber. (G) Percentage of proliferating (eFluor 450-low) and GzB⁺ CD8⁺ T cells in Transwell versus contact coculture (*n* = 3). Representative flow plots show GzB production by CD8⁺ T cells cocultured with E7-loaded mDCs and OX40⁺ or OX40^{lo/-} pDCs in coculture contact or separated by Transwell. (H) Flow plots comparing antigen presentation capacities of autologous OX40⁺ and OX40^{lo/-} pDCs with mDCs, based on cytolytic CD8⁺ T cell responses (no peptide controls for these plots are shown in Supplemental Figure 2B). Shown is GzB production by CD8⁺ T cells in the presence or absence of OX40⁺/OX40^{lo/-} pDCs (top) and IL-12p70 production by mDC/pDC subsets (bottom). *n* = 2; 2 experimental repeats. One-way ANOVA followed by Tukey's post hoc test (C-E and G). Bar graph data are mean \pm SEM; **P* < 0.05. NS, not significant. Middle line of box-and-whisker plot indicates the median, box limits indicate the first and third quartiles, and whiskers indicate "extreme" for all data points. Representative flow plots are shown (C-E and G).

(Figure 3H and Supplemental Figure 2B). Interestingly, in these coculture experiments, E7-loaded OX40⁺ pDCs were also the highest producers of IL-12p70.

Together, these findings demonstrate that OX40⁺ pDCs coordinate with antigen-loaded mDCs to generate potent tumor-specific CD8⁺ T cells in a contact-based fashion and that they can also directly present antigen to CD8⁺ T cells.

The OX40-OX40L axis is utilized by pDCs in the TME. In established tumor models in mice, OX40-expressing DCs have been shown to preferentially bind OX40L in the TME, resulting in their activation (19). We explored the role of OX40L ligation in pDC-mediated antigen-specific CD8⁺ T cell responses by pretreating OX40⁺ pDCs with recombinant OX40L (rOX40L), which dramatically enhanced pDC coordination with mDCs in priming E7-specific

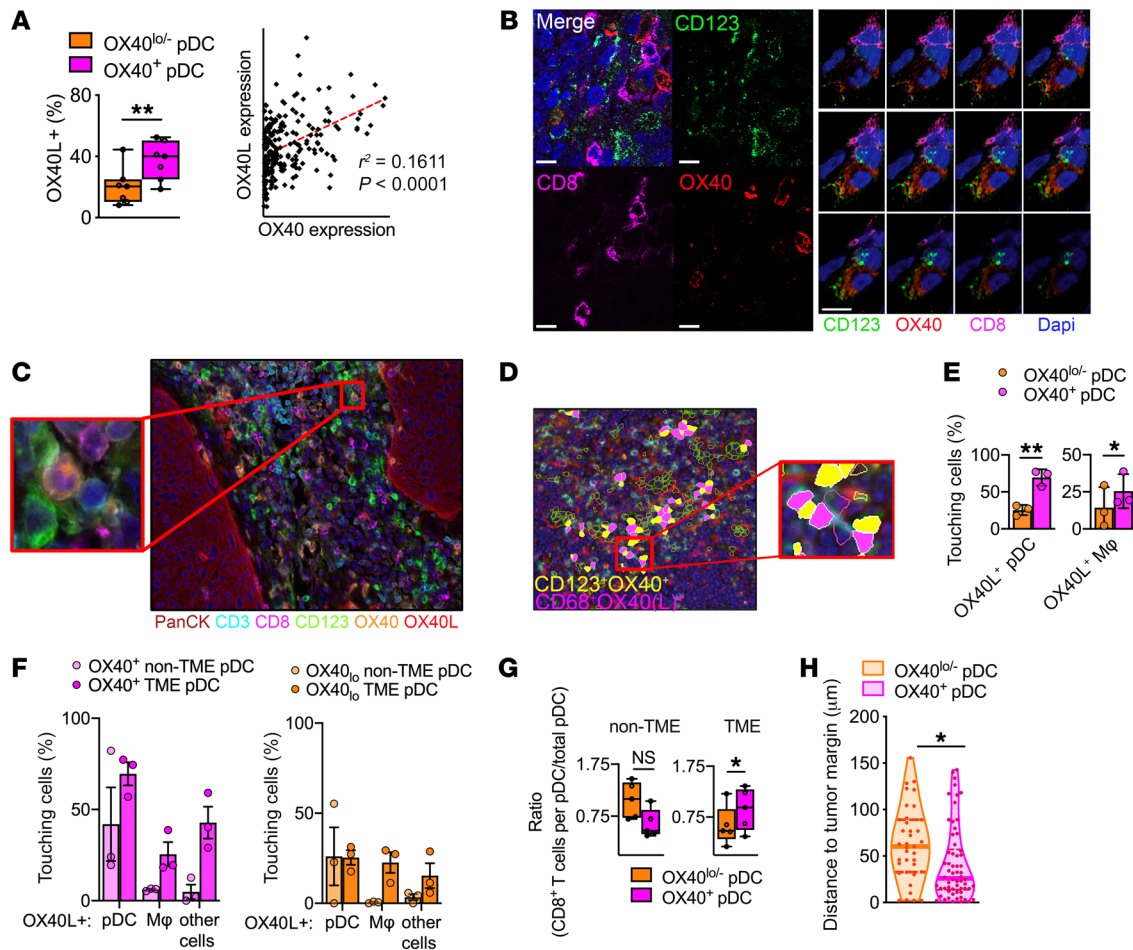


Figure 4. The OX40-OX40L axis is utilized by pDCs in the TME. (A) OX40L expression measured by flow cytometry on OX40⁺ and OX40^{lo/-} pDCs ($n = 7$). Correlation (Pearson, with line of best fit) of OX40 and OX40L expression intensities (per-cell normalized counts, total weighting) on pDCs measured on an HNSCC TME tissue section. $n = 4$; 4 patient repeats. (B) Immunofluorescence images from the TME showing a cell's coexpression of OX40 (red) with CD123 (green), sitting adjacent to CD8-expressing (magenta) cells. Gallery view of Z-stacks (collected at 0.29- μm intervals). Original magnification $\times 63$. Scale bar: 5 μm . $n = 4$; 4 patient repeats. (C) Processed multispectral image (steps outlined in Supplemental Figure 2E for same example image) of the TME. Original magnification $\times 40$. Inset: a cluster CD123⁺ (green) cells, including one with OX40 expression (orange), next to a CD8⁺ (magenta) cell. (D) Representative image file written using Phenopt to calculate touching pairs of phenotyped OX40L⁺CD68⁺ macrophages with phenotyped OX40⁺ pDCs. (E and F) Percentage of phenotyped OX40⁻/OX40^{lo/-} pDCs touching other OX40L⁺ cells, including pDCs, macrophages (M ϕ), and "other cells" (Methods), in the TME and non-TME of patients ($n = 3$). (G) Ratios of CD8⁺ T cell counts within 30 μm of pDC subsets to total counts of CD123⁺ pDC subsets (OX40⁺/OX40^{lo/-}) in the TME and non-TME of patients ($n = 5$). (H) Intercellular distances of phenotyped pDC subsets to the closest tumor margin (μm). Original magnification $\times 40$. $n = 3$; 3 patient repeats. One-way ANOVA followed by Tukey's post hoc test (F) and unpaired (E), and paired (A, G, and H) t tests. * $P < 0.05$; ** $P < 0.01$; NS, not significant. Bar graph data are mean \pm SEM; middle line of box-and-whisker plot indicates the median, box limits indicate the first and third quartiles, and whiskers indicate "extreme" for all data points.

CD8⁺ T cells compared with controls lacking OX40L pretreatment of pDCs (Supplemental Figure 2C). Additionally, treatment of pDCs with combination CpG/Resiquimod and OX40L increased their production of IFN- α compared with treatment with either TLR agonist alone (Supplemental Figure 2D). Correspondingly, combination TLR agonist and OX40L treatment resulted in increased OX40⁺ pDC cytoplasmic secretory granules (Supplemental Figure 2D).

To further explore OX40-OX40L pDC interactions, we determined whether OX40L expression was increased on OX40⁺ pDCs, which would suggest autocrine receptor-ligand interactions. This was confirmed by ex vivo flow cytometric measurement of OX40L expression on sorted pDCs from HNSCC, and using multiplex IHC, we found that intratumoral pDC OX40 and OX40L expression intensities positively correlated to one another (Figure 4A). Next,

we examined matched patient dLN⁺ and dLN⁻ tissue sections for pDC OX40 expression by confocal immunofluorescence microscopy and multiplex IHC (Figure 4, B and C, and Supplemental Figure 2, E and F). Through algorithm-assisted production of image files identifying pDCs "touching" other OX40L-expressing cells (VectraPolaris, Figure 4D), we found that in the TME and compared with OX40^{lo/-} pDCs, OX40⁺ pDCs were significantly more likely to be touching other OX40L⁺ pDCs, as well as OX40L⁺ macrophages (Figure 4, E and F). We also quantified the number of CD8⁺ T cells located within a 30 μm radius of pDC subsets and found that CD8⁺ T cells preferentially clustered around OX40⁺ pDCs only in the TME (Figure 4G). Compared with OX40^{lo/-} pDCs, OX40⁺ pDCs were also more likely to be closer to the tumor based on a shorter intercellular distance to mapped tumor margins (Figure 4H).

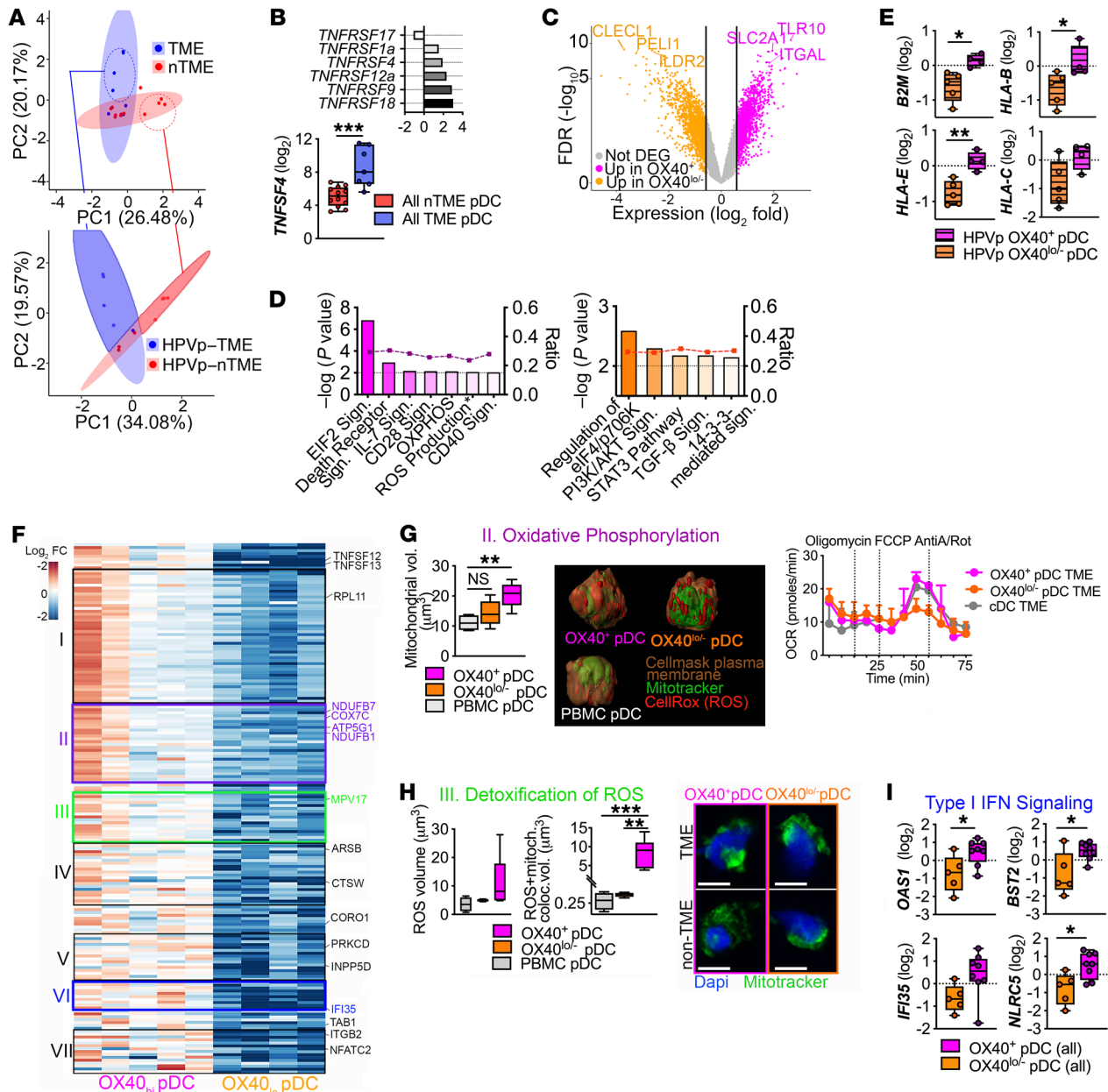


Figure 5. OX40⁺ pDCs harbor a unique transcriptome. (A–F and I) Bulk RNA sequencing was performed on cell-sorted pDCs from HNSCC patients (n = 7) (Supplemental Table 2). DEGs were determined using the criterion of fold changes (FC) greater than or equal to 1.5 (see Methods). (A) Principal component analysis showing the clustering of transcriptional profiles of TME and non-TME pDCs (top), including pDCs from HPV⁺ patients (bottom). (B) Top: log₂ expression of TNF-receptor genes upregulated in the TME of pDC samples. Bottom: expression of *TNFSF4* in the TME versus non-TME pDCs. (C) Volcano plot of gene expression in OX40⁺ pDCs relative to their expression in OX40^{lo/-} pDCs (up- and downregulated in OX40⁺ pDCs colored as magenta and orange, respectively) against the FDR. (D) Top pathways (-log[P value] > 2.0) generated from IPA enriched in OX40⁺ and OX40^{lo/-} pDCs, respectively. Corresponding ratios for each enriched pathway are measured on the second y axis. Full pathway title: Nitrous Oxide and Reactive Oxygen Species Production in Macrophages. (E) Expression of genes involved in MHC I antigen presentation enriched in HPV⁺ HNSCC OX40⁺ pDCs. (F) Heat map reporting relative expression of 183 DEGs in OX40⁺/OX40^{lo/-} pDCs. Gene pathway clusters are demarcated by boxes. (G) Functional correlative data for cluster II (OXPHOS) in OX40⁺ pDCs. Left: Mitochondrial mass measurements in pDC subsets from the TME were calculated using Imaris (see Methods). Original magnification ×100. Scale bar: 5 μm. n = 3; 3 experimental repeats. Right: Real-time analysis of OXPHOS (oxygen consumption ratios measured by Seahorse assay) in sorted pDCs from the TME. n = 2; 2 experimental repeats. (H) Functional correlative data for cluster III (detoxification of ROS): total ROS volumes and ROS colocalized to mitochondria volumes in pDCs from the TME. n = 2; 2 patient experimental repeats. (I) Expression of genes involved in cluster VI (type I IFN signaling) upregulated in OX40⁺ pDCs. Unpaired Student’s *t* test (B and F–I) and right-tailed Fisher’s exact test (E). **P* < 0.05; ***P* < 0.01, ****P* < 0.001; NS, not significant. Error bars represent mean ± SEM of technical duplicates. Middle line of box-and-whisker plot indicates the median, box limits indicate the first and third quartiles, and whiskers indicate “extreme” for all data points. Z scores and genes for IPA in Source Data 1.

These findings indicate that exogenous ligation of OX40 with rOX40L on OX40⁺ pDCs enhances their generation of tumor-specific CD8⁺ T cells and that in the TME, OX40⁺ pDCs are engaged in increased interactions with OX40L expressed on other pDCs as well as macrophages and other cell types.

OX40⁺ pDCs harbor a unique transcriptome. We next sought to characterize the transcriptomes of OX40-expressing pDCs from HNSCC patients for discovery of gene signatures in this pDC subset. Bulk RNA sequencing was performed on FACS-isolated pDC samples ($n = 19$) from the TME and non-TME of HNSCC patients, including sorted OX40⁺ pDC ($n = 8$) and OX40^{lo/-} pDC ($n = 5$) samples (Supplemental Table 2). The quality of RNA-Seq data for all samples was high, and 86.65% of reads were successfully mapped to the human genome.

After filtering and normalizing the raw RNA-Seq data, we ran principal component analysis based on transcriptional profiles per samples. Intriguingly, the divergent distribution patterns revealed in TME pDCs versus non-TME pDCs and in only HPV⁺ TME versus non-TME were consistent, indicating that HPV positivity plays a key role in the genomic differences of these pDC populations (Figure 5A). TNF receptor signaling, including through OX40, was upregulated in TME pDCs across all patients, irrespective of HPV status, as was the expression of *TNFRSF4* (encodes OX40L) (Figure 5B).

A total of 3,495 differentially expressed genes (DEGs) were identified when comparing the genomes of OX40⁺ and OX40^{lo/-} pDC groups, amongst which 1,782 were upregulated and 1,713 were downregulated in OX40⁺ pDCs (Figure 5C). Among the most upregulated DEGs in OX40⁺ pDCs were genes involved in TLR signaling (*TLR10*), immune costimulation and activation (*ITGAL*: encodes CD11a), inflammasome signaling (*PYCARD*, *DNASE1L3*), and glucose uptake (*SLC2A1*: encodes GLUT1). Levels of the master pDC gene regulator *TCF4* were significantly higher in OX40⁺ pDC samples, as were pDC activation genes *IRF8* and *Siglec6*, as well as CD3 ϵ (Supplemental Figure 3A). The most downregulated genes in OX40⁺ pDCs, and thus upregulated in OX40^{lo/-} pDCs, included those involved in IL-4 production by CD4⁺ T cells (*CLECL1*), negative regulation of noncanonical NF- κ B signaling (*PEL1I*), immune cell exhaustion (*ILDR2*), and regulation of antiinflammatory responses (*AHR*, *TSC22*).

Ingenuity Pathway Analysis (IPA) predicted EIF2 signaling, death receptor signaling (including *TNFRSF12A* and *TNFRSF14*), IL-7 signaling, and OXPHOS as the top upregulated canonical pathways in OX40⁺ pDCs and regulation of eIF4/p70S6 and TGF- β signaling among top upregulated canonical pathways in OX40^{lo/-} pDCs (Figure 5D). mTOR signaling — involved in the TCR activation-mediated induction of glucose uptake and glycolysis (20) — was also one of the top upregulated pathways in OX40⁺ pDCs (data not shown). IPA restricted to HPV⁺ OX40⁺ versus OX40^{lo/-} comparisons (Supplemental Figure 3, B and C) was enriched for MHC I signaling (Figure 5E).

Using gene pathway analysis (Kyoto Encyclopedia of Genes and Genomes [KEGG]/Reactome), we clustered 183 upregulated DEGs in OX40⁺ pDCs (Supplemental Table 3 and Figure 5F) according to the following major pathways: (a) TNFSF members mediating noncanonical NF- κ B signaling, EIF2 signaling/ribosome; (b) OXPHOS; (c) detoxification of ROS and peroxisome; (d)

lysosome; (e) phagosome, Fc γ R-mediated phagocytosis; (f) type I IFN signaling; (g) TLR signaling pathway; and (h) NK cell-mediated cytotoxicity (Figure 5, G–I, and Supplemental Figure 3D).

A deeper analysis of OXPHOS in OX40⁺ pDCs from the TME revealed that the mitochondrial volumes of OX40⁺ pDCs were significantly higher compared with autologous peripheral blood pDCs (Figure 5G). Bioenergetics were also measured in pDCs isolated from the TME, and compared with both autologous intratumoral OX40^{lo/-} pDCs and cDCs, OX40⁺ pDCs demonstrated the highest levels of OXPHOS based on their oxygen consumption rate (OCR). Correspondingly, the volume of ROS in OX40⁺ pDCs largely colocalized to their mitochondria, which was significantly greater than that of OX40^{lo/-} pDCs and peripheral blood pDCs (Figure 5H).

A total of 4,197 genes were differentially expressed between pDCs from the HPV⁺ TME and non-TME (Supplemental Table 4). Notable gene pathways upregulated in HPV⁺ TME pDCs across different samples included a combination of innate and adaptive immune responses, including extrinsic signaling pathway via death domain receptor as well as antigen presentation (Supplemental Figure 3E). pDCs from the TME across all patients, irrespective of HPV status, also had higher expression of the CD8⁺ T cell-homing cytokines CXCL8 to CXCL10 (Supplemental Figure 3F). Neither the TME nor OX40 status (data not shown) resulted in consistent pDC genome clustering that would suggest either a common lymphoid progenitor (CLP) or common DC progenitor (CDP) origin (Supplemental Figure 3G).

These results demonstrate that OX40⁺ and OX40^{lo/-} pDCs are transcriptomically distinct on the basis of pathways pertaining to immune costimulation, OX40, and other death receptor signaling, ribosomal protein synthesis, and OXPHOS/ROS generation. Strikingly, the transcriptomes from TME HPV⁺ pDCs are divergent from non-TME HPV⁺ pDCs on the basis of antiviral and CD8⁺ T cell-homing responses.

OX40⁺ pDCs correlate to survival in cancer patients and suppress tumor growth. When further examining the role of OX40 expression on pDCs in the TME in our prospective HNSCC cohort, we found that the presence of OX40⁺ pDCs in the TME was an important predictor of prospective patient survival, as these patients had significantly longer recurrence-free survival (Figure 6A). This also was corroborated by analysis of the overall survival of HNSCC patients in the Genomic Data Commons (GDC) among those with concurrent high pDC gene signatures and levels of *TNFRSF4* (encodes OX40) (Figure 6B). Concurrent high *IL3RA* and *TNFRSF4* levels also corresponded to an increased transcriptomic CD8⁺ effector T cell score in HNSCC patients (Figure 6C).

Because abundant evidence has demonstrated that naturally occurring intratumoral pDCs promote immunotolerance in numerous murine tumor models (3–6, 21), we sought to better characterize the OX40 expression status of intratumoral pDCs and its role in disease behavior in different established murine tumors, including colon (MC38), lung (LLC-OVA), and melanoma (B16-F10 and B16CCR7) (Supplemental Figure 4A and Figure 6D). CCR7 overexpression on tumor cells has been reported to increase the tumor metastasis to dLNs, presumably leading to alterations of the host antitumor inflammatory responses (22). We found that intratumoral pDC expression of OX40 was elevated only in mice bearing established B16CCR7 tumors. We used a

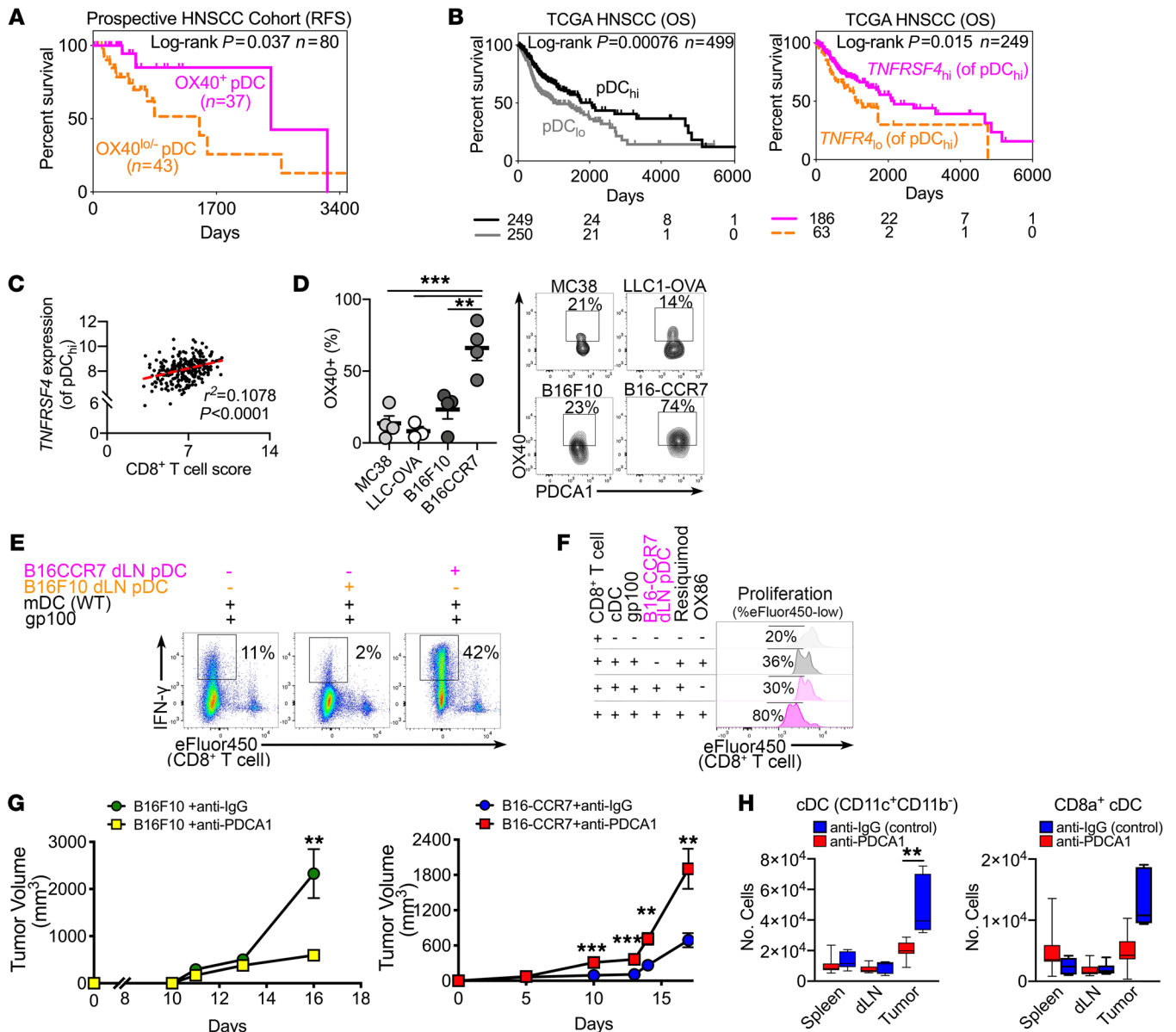


Figure 6. OX40⁺ pDCs correlate to survival in cancer patients and suppress tumor growth. (A) Prospective recurrence-free survival (log-rank, Mantel-Cox test) of HNSCC cohort ($n = 80$), stratified by median (45%) intratumoral pDC OX40 expression, as measured by flow cytometry. (B) Overall survival (log-rank, Mantel-Cox test) of HNSCC patients ($n = 500$) from the GDC data portal, stratified first by median pDC gene signature Z scores followed by stratification of mean *TNFRSF4* (encodes OX40) mRNA levels. (C) Correlation (Pearson, with line of best fit) of *TNFRSF4* log₂ mRNA levels (among cases with pDC_{hi} gene signatures) with CD8⁺ T effector scores in HNSCC ($n = 172$). (D) OX40 expression on intratumoral pDCs from different murine tumor models. $n = 4$; 4 experimental replicates. (E) gp100-specific Pmel-1 CD8⁺ T cell IFN- γ production by proliferating (eFluor 450-low) CD8⁺ T cells, measured in the presence or absence of pDCs from the dLNs of B16-F10- and B16CCR7-bearing mice. $n = 2$; 2 experimental repeats. (F) gp100-specific proliferating (eFluor 450-low) Pmel-1 CD8⁺ T cells in the presence or absence of B16CCR7 pDCs prestimulated with Resiquimod and OX86. $n = 2$; 2 experimental repeats. (G) Effect of pDC depletion (anti-PDCA1) in B16-F10- and B16CCR7-bearing mice compared with controls (anti-polyclonal IgG). Data are pooled from at least 2 independent experiments with 3 to 5 mice per group. (H) Quantification (by flow cytometry) of conventional cDCs (CD11c⁺CD11b⁻) and CD8a⁺ cDCs from B16CCR7-bearing mice treated with anti-PDCA1 or anti-polyclonal IgG. Data are pooled from individual experiments and normalized to 5×10^5 live cells. One-way ANOVA followed by Tukey's post hoc test (D), 2-way ANOVA with Sidak's test for multiple comparisons (H), and unpaired Student's *t* test (G). ** $P < 0.01$; *** $P < 0.001$. Tumor burden data and bar graph data are mean \pm SEM.

murine antigen-specific coculture assay consisting of CD8⁺ T cells from Pmel-1 transgenic mice and gp100-loaded cDCs to study the role of pDCs sorted from the dLNs of B16CCR7 tumors (putative OX40⁺ pDC model) and B16-F10 tumors (putative OX40^{low} pDC model) in cDC priming of CD8⁺ T cells. Similar to OX40⁺ pDCs

from HNSCC patients, only pDCs from the B16CCR7 model synergized with gp100-loaded cDCs to drive gp100-specific CD8⁺ T cell proliferative and cytolytic responses (Figure 6E). The pDCs from the dLNs of B16CCR7-bearing mice also produced higher levels of IL-12p40 when analyzed at the time of coculture harvest,

compared with the pDCs from the dLNs of B16-F10-bearing mice (Supplemental Figure 4B). Likewise, B16CCR7 pDCs from dLNs were sensitive to OX40 ligation; direct stimulation of pDCs with Resiquimod and OX86 (a murine OX40 agonist) significantly increased gp100-CD8⁺ T cell proliferation and production of IFN- γ (Figure 6, E and F) and cDC production of IL-12p40 (Supplemental Figure 4C).

Having established the pDCs from B16CCR7 mice as functional analogues to OX40⁺ pDCs from HNSCC patients, we hypothesized that this population of pDCs was required for control of tumor growth in vivo and further tested this with pDC depletion studies. Whereas depletion of pDCs from B16-F10-bearing mice resulted in significantly lower tumor burden, suggesting they act as modulators of immunotolerance in the TME, in B16CCR7 mice, pDC depletion actually significantly accelerated tumor growth (Figure 6G). In the absence of pDCs, tumors from B16CCR7 mice had a drastic reduction in intratumoral CD11c⁺CD11b⁻ cDCs, including the CD8a⁺ and CD103⁺ cDC subtypes required for effective TAA cross-presentation (Figure 6H and Supplemental Figure 4D). Corresponding analysis of pDC correlation to cDC quantities in tumors from HNSCC patients revealed similar findings — OX40⁺ pDC levels had the strongest positive correlation to the number of intratumoral cDCs compared with OX40^{lo/-} pDCs (Supplemental Figure 4E). pDC-depleted B16CCR7 tumors also had significantly elevated levels of granulocytic (Ly6G⁺) myeloid-derived suppressor cells compared with B16CCR7 control mice, confirmed by immunofluorescence (Supplemental Figure 4, F and G).

Together, these findings demonstrate that the presence of intratumoral OX40⁺ pDCs is a positive predictor of enhanced survival and lower tumor burden in human and mouse tumor models, respectively, and an OX40⁺ pDC-rich tumor model suggests that they are required for the presence of intratumoral cDCs.

Discussion

The presence of tumor-specific CD8⁺ T cell responses in the TME is the underpinning of antitumor immunity and hurdles to its presence include cancer cell immune editing and the expression and secretion of immunoregulatory receptors and cytokines, respectively (23). To date, naturally occurring intratumoral pDCs are considered immunoinhibitory. Here, we characterized a unique pDC subset in the TME of HNSCC, particularly of HPV⁺ patients, defined by expression of OX40^{hi}ICOSL^{lo/null} and that preferentially elicits tumor-specific immune responses. Harnessing the power of naturally occurring immunostimulatory immune populations like these OX40⁺ pDCs is an important means to overcome impediments to the tumor-immunity cycle and to potentially increase the likelihood of patient sensitivity to tumor immunotherapy.

OX40⁺ pDCs represent a morphologically, functionally, and transcriptionally unique population characterized by enhanced immunostimulatory activity. By combining our observations from ex vivo and in vitro experiments using HNSCC specimens and correlative established mouse tumor models to characterize the function of OX40⁺ pDCs, we have created a working 3-way immunological synapse model (see Graphical Abstract) between OX40⁺ pDCs, cDCs, and CD8⁺ T cells. Collectively, our findings offer insight into previous findings that pDCs enhance cDC priming of antigen-specific CD8⁺ T cells and in doing so, protect against

tumor establishment (14, 18). From coculture with autologous mDCs and CD8⁺ T cells, we showed that OX40⁺ pDC enhancement of mDC presentation of antigen to CD8⁺ T cells was contact dependent. We also demonstrated that OX40⁺ pDCs are likely required for the recruitment of CD8a/CD103⁺ cDCs to the TME in an in vivo murine tumor model, and that agonizing the OX40 receptor on pDCs further optimized this effect and increased both cDC and pDC IL-12 production. In line with other findings that pDCs are required for the presence of activated XCR1⁺/CD8a⁺ cDCs in the viral setting (24–26), our findings support a similar role for OX40⁺ pDCs in tumor immunity in mice and in humans. Thus, our work offers complementary mechanistic insight into the enhanced survival outcomes seen in tumor-bearing mice treated with agonistic OX40 treatment (27) that generated antigen-specific CD8⁺ T cells (28), which had been attributed to OX40 expression on T cells but not on other cell types.

Although OX40⁺ pDCs were present in the tumors from HPV⁺ and HPV⁻ HNSCC patients, they were present in the highest concentrations in the tumor metastases from dLNs from HPV⁺ patients. As a subtype of HNSCC that more frequently presents with early cervical lymph node metastases, HPV⁺ HNSCC patients also have an improved clinical outcome (29), and it is interesting to note the increased presence of this pDC population in these patients. We speculate that the OX40 expression on pDCs is upregulated in the presence of HPV. Our results also indicated that OX40⁺ pDCs from HPV⁻ HNSCC patients were comparably capable of producing IFN- α and TRAIL as well as synergizing with mDCs in generating TAA-specific CD8⁺ T cells, indicating that the immunostimulatory properties of OX40⁺ pDCs are not limited to viral-driven HNSCC.

Our transcriptomic data showed that OX40⁺ pDCs had selective transcription of the pDC-defining genes *IRF8* and *E2-2 (TCF4)* and preferential expression of genes relating to antigen presentation (CD40, CD80, CD86, OX40L, TLR signaling). In the viral setting, pDCs are capable of cross-presenting viral antigen to CD8⁺ T cells (30, 31) and in this study, we showed that pDCs, particularly OX40⁺ pDCs, were capable of cross-presenting tumor peptide (in our case HPV E7 pp11-19) to CD8⁺ T cells. Although little data exist to demonstrate that pDCs process protein antigen, our RNA-Seq findings indicated that OX40⁺ pDCs from HPV⁺ HNSCC patients had transcriptomes enriched in expression of *HLA-B*, *HLA-E*, and *B2M* genes, Fc γ R-mediated phagocytosis, and lysosome signaling, suggesting that they engage in the phagocytosis, processing, and presentation of exogenous tumor antigen. In this vein, OX40⁺ pDCs shared some but not all features of the previously identified CD2⁺CD5⁺ pDC subset (32, 33), including their enhanced ability to directly present antigen to autologous CD8⁺ T cells, increased production of IL-12, and high expression of the myeloid gene *LYZ* (data not shown).

Our canonical pathway analysis also demonstrated that OX40⁺ pDCs from the TME preferentially utilized mitochondrial OXPHOS as an energy source. This unique metabolic profile of this pDC subset draws comparisons to the recently identified energy demands of NKT cells, which also utilize OXPHOS as a vital energy source for their survival, proliferation, and cytotoxicity (34). Further investigation is needed to identify the glucose requirements of OX40⁺ pDCs because *SLC2A1* (encodes Glut1) was one of the most upregulated DEGs in this pDC subset and

because mTOR signaling — involved in the TCR activation-mediated induction of glucose uptake and glycolysis (20) — was one of the top upregulated pathways in OX40⁺ pDCs.

Another gene pathway we found enriched in OX40⁺ pDCs pertained to T cell functions (CD28, OX40, CD25, IL-12, IL-7R) and in our canonical signaling analysis, we found that OX40⁺ pDCs were also enriched for death receptor/IL-7/CD28/CD40 signaling. Recent work on pDC ontogeny has identified IL-7R α ⁺ CLP as giving rise to a subset of pDCs enriched in the expression of lymphoid-associated genes (35–37). Although we showed that IL-7R signaling was enriched in OX40⁺ pDCs, our finding that OX40⁺ pDCs were functionally more effective in antigen presentation supports a myeloid precursor lineage. Thus, OX40⁺ pDCs were transcriptomically unique for dual expression of CDP and CLP lineage-based expression profiles. We infer from these findings that OX40⁺ pDCs undergo transcriptomic plasticity in the TME rather than commitment along a single progenitor lineage.

Although the mechanism of OX40 signaling in cells that lack a TCR remains unclear, it is important to note that unlike other costimulatory molecules, TCR ligation alone is insufficient to upregulate OX40 expression and it is also upregulated by cytokine signaling systems such as IL-2/IL-2R (38, 39). In this study, we found that CD25/IL-2RA, one of the subunits of the high-affinity trimeric IL2R complex, was preferentially expressed on OX40⁺ pDCs and that treatment of pDCs with IL-2 increased their overall OX40 expression. Interestingly, coculture of pDCs with HNSCC tumor cell lines resulted in pDC activation and expression of CD25 as well as some other TNFR proteins (e.g., GITR), invoking a possible specialized phenotype in HNSCC (40), comparable to our findings.

In addition to increased induction of IFN- α , OX40⁺ pDCs also produced greater levels of TRAIL and GzB in response to TLR7/8 and/or TLR9 stimulation, suggesting they may have a greater capacity to directly kill tumor cells, independent of adaptive immunity, supported by previous work on TLR-activated pDCs in established tumor models (13). pDC combination treatment with CpG/Resiquimod and rOX40L yielded higher IFN- α levels than TLR-agonist monotherapy. OX40L has been characterized on pDCs in tumor immunity as having mixed immunoinhibitory and immunostimulatory roles (14, 17, 41, 42). OX40/OX40L signaling has also previously been implicated in type I IFN production by pDCs, and abrogation of OX40L signaling greatly reduced pDC IFN- α production (41). In multiplex IHC analysis of the TME in HNSCC, we identified selective cell-to-cell contact between OX40⁺ pDCs and cells expressing OX40L, notably other pDCs. We also showed that similarly to treating human pDCs, treating murine pDCs from the dLNs of B16-CCR7-bearing mice and B16-F10-bearing mice (data not shown) with a combination of OX86 and Resiquimod was more effective in driving antigen-specific proliferation of Pmel-1 CD8⁺ T cells than the addition of pDCs stimulated with only Resiquimod.

Collectively, these findings demonstrated that pDC OX40-OX40L signaling mediates immunostimulatory effects and that in vivo in the TME, the OX40/OX40L-signaling axis likely increases local IL-12 and IFN- α production and enhances cDC and CD8⁺ T cell interactions. Correlative studies in the mouse system were initially challenged by the fact that intratumoral pDCs from multiple

tumor models, including LLC1 lung cancer, MC38 colon cancer, and B16-F10 melanoma expressed very low levels of OX40 and would not serve as an appropriate corresponding model to our findings in human HNSCC. Low OX40 expression on intratumoral pDCs in these models is viable justification for their already established inhibitory functions in numerous tumor models and pDC depletion experiments, including our own depletion experiments in this study on B16-F10 melanoma (43–45). However, in identifying the B16CCR7-expressing melanoma model as containing intratumoral pDCs with high levels of OX40 expression, we were able to further study the role of this unique immunostimulatory pDC population in tumor development.

Up until this point, no naturally occurring intratumoral immunostimulatory subset of pDCs has been characterized. Our discovery of OX40⁺ pDCs, which accumulate most dramatically in the tumors and dLNs from HNSCC patients, calls for reexamination of our classification of the role of pDCs in tumor immunity. Future work is necessary for the discovery of therapeutic means to upregulate OX40 expression on intratumoral pDCs in order to effectively induce both innate and adaptive antitumor immunity.

Methods

Human research samples and creation of single-cell suspensions. Tumor and nontumor tissues were collected during standard surgical procedures from the Department of Pathology, Northwestern Memorial Hospital. Tumor-node-metastasis (TNM) staging of patients with HNSCC was determined using the eighth edition of the AJCC Cancer Staging Manual. Tumor and lymph node tissues not needed for diagnostic purposes were cut into small pieces and digested as previously described (46). In brief, a uniformly sized portion of fresh tissue (0.5 cm³) was harvested from either grossly visible tumor and/or matched uninvolved cervical lymph nodes within one hour of resection and transported in either RPMI or DMEM at room temperature for immediate enzymatic digestion. PBMCs were obtained from blood (5–15 mL) collected in heparinized tubes, either preoperatively or intraoperatively, using SepMate-50 PBMC isolation tubes (StemCell Technologies).

Antibodies, flow cytometry, and cell sorting. All staining of single cell suspensions was done following internal validation by titrating using tonsil or PBMCs from healthy donors. For a complete list of antibodies used in staining panels, refer to Supplemental Table 5.

For measurement of IFN- γ and GzB in coculture experiments, cells were incubated with 50 ng/mL PMA (50 ng/mL) and ionomycin (5 μ g/mL) in the presence of BFA (10 μ g/mL) RPMI at 37°C for 4 to 6 hours. Intracellular staining was performed as previously described using BD Cytotfix/Cytoperm (46). For Foxp3 staining, cells were fixed and permeabilized using eBioscience Foxp3 staining buffer set. For coculture experiments, fresh autologous CD8⁺ T cells isolated from peripheral blood were labeled with cell proliferation dyes eFluor 450 (Thermo Fisher Scientific) per the manufacturer's protocol. In experiments analyzing mDC function, mDCs were labeled with eFluor 670 (Thermo Fisher Scientific) prior to coculture with autologous CD8⁺ T cells and pDCs.

Flow cytometric immunophenotyping was performed on a BD LSRFortessa analyzer at the Northwestern University Robert H. Lurie Comprehensive Cancer Center (RHLCCC) Flow Cytometry Core Facility and data sets were analyzed using FlowJo software (version 10, Tree Star). Cells were sorted on BD FACSAria 4-, 5-, and 6-laser

sorters at the RHLCCC Flow Cytometry Core Facility using the purity mode, a 100- μ m nozzle loop, and at low pressure (20 psi). Based on cell number, either whole pDCs or OX40⁺ and OX40^{lo/-} pDC subsets were sorted (1×10^3 to 12×10^4 pDCs based on the sample). For RNA-Seq experiments, cells were directly sorted into lysis buffer LB1 (NucleoSpin RNA Plus XS, Macherey-Nagel) supplemented with RNase Inhibitor (SUPERase-In, Invitrogen, 200 U/ μ L), and RNA was immediately isolated.

Morphological analysis. Sorted cells were cytospun onto glass slides and stained with May-Grunwald-Giemsa stain. Images were obtained with a Nikon Eclipse E800 microscope with an Axiocam HR camera and analyzed using AxioVision software (Carl Zeiss).

Immunofluorescence. Tumor tissue from HNSCC patients was flash frozen in OCT (Thermo Fisher Scientific) and sectioned into 6- μ m slices. Sections were fixed and permeabilized in a 1:1 acetone/methanol solution for 20 minutes at -20°C and blocked in blocking buffer (5% BSA/2.5% normal goat serum in PBS) for 45 minutes at 37°C . Tissue sections were incubated for 1 hour in blocking solution at 4°C with the following primary antibodies: rat anti-human CD8 (1:200, clone: YTC182.2, Bio-Rad), mouse anti-human CD123 (1:75, clone: 7G3, BD), and rabbit anti-human OX40 (1:80, E9U70; Cell Signaling Technology). For analysis of mouse tumors, rat anti-mouse Ly-6G and Ly-6C (1:200, clone: RB6-8C5, BD) were used. Tissue sections were washed 3 times in PBS and then stained with the following goat secondary antibodies for 45 minutes at 37°C : anti-rabbit IgG Alexa Fluor 568 (1:250, Abcam, ab175471), anti-mouse IgG Alexa Fluor 488 (1:250, BioLegend), and anti-rat IgG Alexa Fluor 647 (1:250, Thermo Fisher Scientific, A-21247). After 3 washes in PBS, sections were stained with DAPI (Sigma-Aldrich) for 2 minutes at 37°C and mounted with SlowFade Diamond Antifade (Thermo Fisher Scientific). Images were generated using an AxioImager Z2 microscope (Carl Zeiss) equipped with EC Plan-Apochromat $\times 10$ (NA 0.45), $\times 20$ (NA 0.8), $\times 40$ (NA 1.4), and $\times 63$ (NA 1.4) objectives, with X-Cite 120 LED Boost System, an ApoTome 2 attachment, a digital camera (Axiocam MRm, Carl Zeiss), and analyzed using ZEN 2.3 software (Carl Zeiss).

For imaging of pDC mitochondria, FACS-isolated pDCs were stained with MitoTracker Green FM (Thermo Fisher Scientific) and/or CellROX Deep Red (Thermo Fisher Scientific) and CellMask Orange plasma membrane stain (Thermo Fisher Scientific), and then suspended in RPMI 1640 medium, no phenol red (Thermo Fisher Scientific) precoated with poly-D-lysine hydrobromide (100 μ g/mL, Sigma-Aldrich). In cases where pDCs were only stained with MitoTracker, cells were fixed and permeabilized followed by staining with DAPI before imaging. Cells were imaged at the Northwestern University Center for Advanced Microscopy using a Nikon A1 confocal microscope equipped with GaAsP detectors, a $\times 100$ Plan-Apochromat objective lambda with an NA of 1.4 and analyzed in NIS-Elements (version 4.0, Nikon). 3D rendering and volumetric analysis of pDC mitochondrial volume was performed with Imaris 9.2 (Bitplane). Images were further processed using Photoshop CC (version 20.0.1, Adobe).

In vitro stimulation of pDCs in cell culture. Sorted pDC subsets were cultured in 96-well round-bottom plates with RPMI medium containing 10% FBS, 2 mM L-glutamine, 100 units/mL penicillin and streptomycin, 1 mM sodium pyruvate, and 10 mM HEPES. pDCs were stimulated with TLR9 agonist class B CpG oligonucleotide (ODN 7909, Sigma-Aldrich) (0.5 μ M), TLR7/8 agonist Resiquimod

(1 μ g/mL, InvivoGen), recombinant, carrier-free IL-2 (0.2 ng/mL, BioLegend), and/or recombinant carrier-free human OX40L (0.5 μ g/mL, BioLegend). For mouse pDC stimulation, OX86 was used (1 μ g/mL, Thermo Fisher Scientific).

Measurement of cytokines. Supernatants from the stimulation of pDCs were analyzed with ELISA for IFN- α (Human IFN- α Platinum ELISA kit, Invitrogen) or by Luminex for IFN- α , GzB, and TRAIL (custom-built, R&D). For the latter, the Luminex 200 instrument was used (MilliporeSigma).

Peptides. In autologous coculture experiments, mDCs were loaded with HLA class I:A2-restricted peptides (all 5 μ g/mL). CMV pp65 (Astarte Biologics) was used as an assay control. For HPV⁺ HNSCC patients, HPV 16 epitope E7¹¹⁻¹⁹ (Bio-Synthesis Inc), an established HPV epitope (47) recognized by CD8⁺ T cells in HPV-driven carcinomas, was loaded onto mDCs. For HPV⁻ HNSCC patients, EGFR^{479-488,1138-1147} or Her2³⁶⁹⁻³⁷⁷ were used, as both have been reported as antigens targeted by CD8⁺ T cells in HNSCC (48-50). For mouse coculture experiments, hgp100²⁵⁻³³ (GenScript) was used. Peptides were dissolved in either water or DMSO per the manufacturer's instructions.

Analysis of HNSCC patient CD8⁺ T cell responses in coculture with autologous pDC subsets. CD8⁺ T cells from HNSCC patient PBMCs obtained from blood provided the day of the surgery were isolated by immunomagnetic negative selection using EasySep Human CD8⁺ T Cell Enrichment kit (StemCell) and then labeled with eFluor 450. mDCs were generated following a cytokine-based differentiation protocol (51). Monocytes isolated from fresh blood obtained from HNSCC patients in clinic during their preoperative appointments were isolated using EasySep Human Monocyte Isolation Kit (StemCell). Isolated monocytes were cultured in 24-well plates (1×10^6 cells/well) in DC medium (ImmunoCult-ACF Dendritic Cell Medium, StemCell), which was replaced every 2 days, consisting of 2 mM alanyl-glutamine (GlutaMax, Thermo Fisher Scientific) and cytokines, all from BioLegend, including IL-4 (10 ng/mL) and GM-CSF (10 ng/mL). Forty-eight hours before the patient's surgery, mDCs were matured with TNF- α (5 ng/mL), IL-1 β (10 ng/mL), and IL-6 (100 ng/mL). Approximately 12 hours prior to the surgery, the DCs were harvested using an enzyme-free PBS dissociation buffer (Thermo Fisher Scientific) and were stained for HLA-A2. A small aliquot was stained and evaluated by flow for maturation status (HLA-DR, CD80, and CD86). HLA-A2⁺ mDCs were FACS isolated and plated onto 96-well flat-bottom plates at 10×10^4 to 20×10^4 mDCs/well in ImmunoCult DC medium. mDCs were loaded with 5 μ g/mL of either control peptide or TAA-peptide, customized to the patient's HPV status.

In antigen-independent assays, sorted OX40⁺ or OX40^{lo/-} pDCs from patient tissue samples were cocultured with peripheral blood CD8⁺ T cells for 72 hours with CD3/CD28 T cell activator (StemCell) in ImmunoCult-XF T cell expansion medium (StemCell), supplemented with 100 units/mL penicillin and streptomycin and IL-2 (0.2 ng/mL) at a stimulator-to-responder (S/R) ratio of 1:5 to 10. For the autologous antigen-specific coculture assay utilizing mDCs, after 2 hours of peptide loading and washing of mDCs, CD8⁺ T cells were added to the mDCs and to prestimulated, sorted OX40⁺ or OX40^{lo/-} pDCs from the TME/dLN/PBMC (stimulated overnight with either CpG or Resiquimod) at a T cell/mDC ratio of 1:5 to 10 and a T cell/pDC ratio of 1:10 in ImmunoCult-XF T cell expansion medium for 6 to 7 days, supplemented with 100 units/mL penicillin and streptomycin and IL-2 (0.2 ng/ μ L).

In experiments designed to compare the antigen presentation capacities of OX40⁺ or OX40^{lo/-} pDCs with autologous mDCs, mDCs, OX40⁺ pDCs, and OX40^{lo/-} pDCs were all separately preloaded with TAA-peptide (5 µg/mL) and washed prior to separately coculturing with autologous CD8⁺ T cells at an S/R ratio of 1:10 in ImmunoCult-XF T cell expansion medium for 6 to 7 days, supplemented with 100 units/mL penicillin and streptomycin and IL-2 (0.2 ng/µL).

Transwell studies. Sorted pDC subsets were added to the top chamber of 0.4-µm 96-well Transwell plates (Corning HTS, MilliporeSigma), with the lower chamber containing autologous peptide-loaded mDCs and eFluor 450-labeled CD8⁺ T cells. After 6 to 7 days of incubation, antigen-specific CD8⁺ T cell responses were measured and compared with CD8⁺ T cell responses from wells that contained CD8⁺ T cells, peptide-loaded mDCs, and pDC subsets in contact.

Multiplex IHC. Multiplex IHC staining was performed on 4-µm FFPE tissue sections from matched HNSCC patient tumors and dLN^s using the Opal 7-Color Manual IHC Kit (NEL861001KT; Akoya Biosciences). Sections were deparaffinized and tissue was fixed with 10% neutral buffered formaldehyde. Antigen recovery (AR) using pH6 citrate buffer or pH9 EDTA buffer and primary anti-human antibodies and concentrations were optimized as follows: CD8a (1:400; C8/144B, Cell Signaling Technology; AR9), CD3 (prediluted, EP41; Biocare Medical; AR6), CD123 (1:500, 7G3; BD Biosciences; AR9), OX40 (1:100, E9U7O; Cell Signaling Technology; AR9), OX40L (1:200, D6K7R; Cell Signaling Technology; AR9), and pan-cytokeratin (panCK) (1:50, AE1/AE3; Abcam; AR6). In a subset of matched patient tumor and dLN⁻ tissue sections that were analyzed for OX40L touching-cell analysis (see next section), CD68 (prediluted, KP1; Biocare Medical; AR9) was used in place of CD8 primary antibody. All slides were counterstained with Spectral DAPI (1:10, Akoya Biosciences; AR6) nuclear stain and mounted with Slowfade Diamond Antifade mountant (Thermo Fisher Scientific).

Multispectral imaging and analysis. After staining single FFPE tissue sections using opal fluorophores against 8 markers, we performed multispectral imaging using the Vectra Polaris (Akoya Biosciences) automated quantitative imaging system at the University of Chicago Human Immunologic Monitoring Facility. In brief, images were acquired at ×4 original magnification, from which regions of interest (ROI) were selected (approximately 15–20 per scanned tissue section) based on areas of tumor or lymphoid tissue with adequate distribution of different cell populations captured by the different markers. Using Nuance software (version 3.0.2, Akoya Biosciences), these ROI were then captured in Nuance at ×20 and ×40 original magnification, and raw ROI images underwent a process called “spectral unmixing” into individual emitting spectral peaks for all 8 fluorophores (52, 53), which became part of a “spectral library.” The creation of the spectral library allowed for spectral unmixing of all collected ROI raw images, followed by a proprietary active learning phenotyping algorithm using inForm Advanced Image Analysis software (2.4.1 Akoya Biosciences). Using this algorithm, images were subjected to tissue segmentation (into tumor and stroma), cell segmentation, and phenotyping tools, such that each DAPI-stained cell was identified and phenotyped according to its fluorophore expression and placed at its specific *x*, *y* spatial coordinates.

inForm was trained to create the following phenotypes: tumor cells (panCK⁺), pDCs (CD3⁺CD123⁺), macrophages (CD68⁺), CD8⁺ T cells (CD3⁺CD8⁺), and “other cells” (panCK⁺CD68⁺CD8⁺CD123⁺). All

settings were saved as an algorithm to enable batch analysis of ROI images from matched patient tumors and dLN^s, and analysis of each ROI captured at ×20 and analyzed in inForm was performed using exported Excel cell segmentation tables and the R package Phenoptr (Akoya Biosciences) (54) to (a) define new phenotypes that characterize phenotyped pDCs as OX40⁺ or OX40^{lo/-} based on upper and lower quartile OX40 expression values, as well as define phenotyped pDCs, macrophages, and “other cells” as positive for OX40L based on median OX40L expression values; (b) compute the intercellular distances of OX40⁺ or OX40^{lo/-} pDCs to the nearest tumor margin (determined from tissue segmentation) based on *x* and *y* coordinates; and (c) count phenotyped CD8⁺ T cells within a 30-µm radius from phenotyped pDCs for a single field. Phenoptr was also used to write image files of touching cells from cell segmentation tables, image binary segmentation maps, and composite images to count touching cells from phenotyped OX40⁺ or OX40^{lo/-} pDCs with phenotyped OX40L⁺ pDCs/macrophages/“other cells.”

RNA isolation and sequencing. RNA from FACS-isolated cells (≥8,000) was extracted using a low-input RNA isolation kit (NucleoSpin RNA Plus XS, Macherey-Nagel), including on-column DNase digestion as described by the manufacturer’s protocol. The RNA of each sample was quantified using the Qubit RNA HS Assay Kit (Thermo Fisher Scientific), and RNA integrity was evaluated using an RNA 6000 Pico Kit (Agilent Technologies) in 2100 Bioanalyzer (Agilent Technologies). mRNA was isolated using the NEBNext Poly(A) mRNA Magnetic Isolation Module (New England Biolabs), and cDNA libraries were generated using the low-input strand-specific RNA-Seq kits NEBNext Ultra II RNA Library Prep Kit for Illumina (96 reactions) and NEBNext Multiplex Oligos for Illumina (96 index primers) (New England Biolabs). All RNA and DNA purification steps were performed using AMPure XP Beads (Beckman Coulter Inc.). The quantity and quality of cDNA were assessed using the Qubit dsDNA HS Assay Kit (Thermo Fisher Scientific). Libraries were sequenced in the same batch at Northwestern University Sequencing Core (NUSeq) in the Illumina NextSeq500 (75SE High Output) platform using single-end 75-bp reads and generating on average 20 million reads per sample. The quality of raw reads was assessed by the FastQC (version 0.11.7).

RNA-Seq data processing. All RNA-Seq data processing was done at the Bioinformatics Core, Center for Research Informatics at the University of Chicago Biological Sciences Division. Dimensionality reduction, an informative approach for clustering and exploring the relationships between samples, was performed with principal component analysis plot based on the normalized mRNA expression profiles. Reads were mapped to the human genome reference (hg38) using the STAR version 2.5.4b (55) release with default parameters. Picard version 2.8.1 (<http://broadinstitute.github.io/picard>) was used to collect mapping metrics. The resulting files from the previous alignment step were taken as input to quantify transcriptional expression using featureCounts (Rsubread, version 1.28.1) (56). Three state-of-the-art tools of differential expression analysis were used to identify DEGs between pairwise groups, including DESeq2 (57), edgeR (58), and limma (59). To identify a more robust collection of intrinsically regulated genes, the overlapped DEGs detected by more than one method were considered as the final set of DEGs for further analysis. The following 4 pairwise comparisons were performed for DEG determination using the criterion of fold changes greater than or equal to 1.5: (a) TME (*n* = 7) versus non-TME (*n* = 12), (b) HPV⁺ TME (*n* = 5) versus HPV⁺ non-TME

($n = 7$), (c) OX40⁺ ($n = 8$) versus OX40^{lo/-} ($n = 5$), and (d) HPV⁺ OX40⁺ ($n = 4$) versus HPV⁺ OX40^{lo/-} ($n = 4$). Several in-house scripts were implemented using R (<http://www.r-project.org>) and Python (<http://www.python.org>) languages to obtain clusters with similar expression trends based on identified DEGs. For heat maps, DEGs were shown as log₂-transformed fold changes to the mean normalized expression of the control group.

Gene set analysis and gene set enrichment analysis. The identified DEGs were further used as input to functional analysis for the identification of enrichment of functional categories and regulatory networks, using Gene Ontology (GO) terms and KEGG. Pathways significantly enriched in the genes of interest were identified using clusterProfiler (version 3.6.0) at an FDR-adjusted P value of less than 0.10 (hypergeometric test) (60). Gene set enrichment analysis (GSEA) was performed using clusterProfiler (version 3.6.0) as well. DEGs were also subjected to KEGG and REACTOME pathway enrichment analysis using DAVID (6.8) (61, 62), and only pathways with P values under 0.05 were kept.

Pathway enrichment analysis. Functional analysis of genes with statistically significant expression changes was performed for biological functions and canonical pathways using the Ingenuity Pathways Knowledge Base (IPKB) in IPA (QIAGEN Inc.). Only pathways with a Benjamini-Hochberg-adjusted P value under 0.05 were presented as enriched. For IPA of OX40⁺ pDCs and OX40^{lo/-} pDCs, OX40⁺ pDCs were used as experimental samples in IPA with corresponding negative Z scores, and OX40^{lo/-} pDCs were used as controls with corresponding positive Z scores generated. Z scores, which take into account the direction of change of molecules in the data set, were calculated in the IPA software based on the data set's correlation with the activated state.

Mitochondrial stress test measuring OCR. Sorted pDC subsets and mDCs from the TME of HNSCC patients were immediately adhered to a Seahorse XF96 cell culture microplate (Agilent) with Cell Tak (Corning) at a density of 2.0×10^4 cells/well. The OCRs were measured in XF RPMI Seahorse medium supplemented with 10 mM glucose and 2 mM L-glutamine in response to oligomycin (2 μ M), FCCP (1 μ M), rotenone (100 nM), plus antimycin (4 μ M) (Sigma-Aldrich).

Analysis of data from cancer patients in GDC data portal. For the GDC data portal (<http://portal.gdc.cancer.gov>), level 4 gene expression data and clinical data were downloaded via the GDC R library (63, 64) (accessed January 2019) for HNSCC ($n = 500$). Gene expression was determined using log₂ transformation of raw counts normalized in DESeq2. pDC gene signatures were determined by averaging the normalized expression of *CLEC4C*, *TCF4*, and *GZMB* and using the median Z score as the cutoff for high and low. Patients with high pDC gene signatures were then stratified by mean *TNFRSF4* expression levels for Kaplan-Meier survival analysis (log-rank, Mantel-Cox test). CD8⁺ T effector scores were generated as previously reported (65) and were formed from an average of normalized and transformed expression values of the following genes: *CD8A*, *CD8B*, *IFNG*, and *PRF1*. Correlation of CD8⁺ T effector scores with normalized log₂-transformed *TNFRSF4* levels was determined using the Pearson correlation coefficients.

Mouse experiments. C57BL/6 and Pmel-1 mice, 6 to 8 weeks old, were purchased from The Jackson Laboratory. Hans Schreiber (University of Chicago) provided B16F10 and MC38 cell lines, and Sam T. Hwang (Medical College of Wisconsin) provided the B16-CCR7 cell line. The LLC-OVA cell line has been described previously (66). All

the cell lines were routinely tested for mycoplasma infections by culture and DNA stains and maintained in complete medium composed of DMEM supplemented with 10% FBS at 37°C in a 5% CO₂ incubator.

B16-F10 and B16-CCR7 cells (2×10^5) in suspension were injected subcutaneously into the rear right flank of mice. Depletion of pDCs was achieved by i.p. injection with depleting mAb clone CD317/BST2/PDCA1 (BioXCell BE0311) or polyclonal isotype control (BioXCell BE0094) every 2 to 3 days (first dose: 500 μ g; subsequent doses: 250 μ g), including 1 day prior to tumor challenge. Splenic CD8⁺ T cells from Pmel-1 mice were selected using EasySep Mouse CD8⁺ T Cell Isolation Kit (StemCell, 19853). Splenic DCs from C57BL/6 mice were selected using EasySep Mouse CD11c Positive Selection Kit II (StemCell, 18780).

Data availability. The data sets generated during the current study are available in the form of source data. All RNA-Seq transcriptional profiles of pDC populations from HNSCC patients in this study are provided as a resource and are available through dbGAP (<https://www.ncbi.nlm.nih.gov/gap>) in the NCBI Sequence Read Archive (SRA) with the SRA ID SRP199931.

Statistics. Data analysis was performed using GraphPad Prism (version 8.1.0) for statistical analysis to compare outcomes using a 2-tailed paired and unpaired Student's t test. For multiple comparisons, 1-way ANOVA and 2-way ANOVA were performed. Correlation analysis was performed by determining Pearson correlation coefficients. For patient survival analysis, progression-free survival distributions were estimated using the Kaplan-Meier method and compared with the log-rank test. P values of less than 0.05 were considered to be statistically significant.

Study approval. Human studies were part of a protocol approved by the Internal Review Board of Northwestern University. Written informed consent was obtained from all participants and/or their legal guardians from patients undergoing surgery from December 2015 to January 2019. Samples came from patients between the ages of 30 and 81. All animal procedures were approved by the IACUC at Northwestern University.

Author contributions

KP and BZ designed the project and interpreted the data. KP wrote the manuscript. KP, DD, JM, LQ, and LC performed experiments. KP, BW, and WCC performed statistical analysis. WCC, BW, and JA analyzed RNA-Seq data. SC, UP, and SS provided clinical samples. YZ helped interpret multiplex IHC data and provided technical expertise. All authors agreed to submission of the manuscript for publication.

Acknowledgments

We thank Cheryl Olson (Department of Pathology, Northwestern University) and David Klrchenbuechler (Northwestern University's Center for Advanced Microscopy) for their assistance in AxioVision and Imaris programs, and Suchitra Swaminathan, Paul Mehl, and Darryl Abbott (all at the Northwestern University RHLCCC) for their assistance with FACS. We are grateful to Jessica Ania from the Northwestern Memorial Hospital Department of Pathology for coordinating the access to surgical specimens. We thank Tiffany Nicole Johnson and Hanli Fan for their assistance in providing peripheral blood from patients. We thank Kristy Skurauskis for her assistance in tissue acquisition and Maria Montano

and Kristyn Mickley for their assistance in obtaining patient preoperative peripheral blood. We also acknowledge the following facilities for completion of experiments performed in this study: Northwestern University's Center for Advanced Microscopy, Sequencing Core; RHLCCC Flow Cytometry Core; RHLCCC Immune Assessment Core and Mouse Immunophenotyping Core; and University of Chicago's Human Immunologic Monitoring Facility and Center for Research Informatics. This study was supported by the Riviera Foundation United-4-a-Cure Award; NIH grants U54CA199091, R01CA208354, and R01CA222963; and a Flow Cytometry Core

Facility Cancer Center Support Grant (NCI CA060553). Flow cytometry cell sorting was performed on a BD FACSAria SORP system, purchased through the support of NIH 1S10OD011996-01.

Address correspondence to: Bin Zhang, Tarry Building Room 4-725, 300 East Superior Street, Chicago, Illinois 60611, USA. Phone: 312.503.2447; Email: bin.zhang@northwestern.edu. Or to: Kate Poropatich, 251 East Huron Street, Feinberg Pavilion 7-330, Chicago, Illinois 60611, USA. Phone: 301.233.3533; Email: kate.poropatich@gmail.com.

- Liu YJ. IPC: professional type 1 interferon-producing cells and plasmacytoid dendritic cell precursors. *Annu Rev Immunol.* 2005;23:275-306.
- Reizis B. Plasmacytoid dendritic cells: development, regulation, and function. *Immunity.* 2019;50(1):37-50.
- Conrad C, et al. Plasmacytoid dendritic cells promote immunosuppression in ovarian cancer via ICOS costimulation of Foxp3(+) T-regulatory cells. *Cancer Res.* 2012;72(20):5240-5249.
- Labidi-Galy SI, et al. Quantitative and functional alterations of plasmacytoid dendritic cells contribute to immune tolerance in ovarian cancer. *Cancer Res.* 2011;71(16):5423-5434.
- Wei S, et al. Plasmacytoid dendritic cells induce CD8⁺ regulatory T cells in human ovarian carcinoma. *Cancer Res.* 2005;65(12):5020-5026.
- Hartmann E, et al. Identification and functional analysis of tumor-infiltrating plasmacytoid dendritic cells in head and neck cancer. *Cancer Res.* 2003;63(19):6478-6487.
- Sisirak V, et al. Breast cancer-derived transforming growth factor- β and tumor necrosis factor- α compromise interferon- α production by tumor-associated plasmacytoid dendritic cells. *Int J Cancer.* 2013;133(3):771-778.
- Sisirak V, et al. Impaired IFN- α production by plasmacytoid dendritic cells favors regulatory T-cell expansion that may contribute to breast cancer progression. *Cancer Res.* 2012;72(20):5188-5197.
- Zou W, et al. Stromal-derived factor-1 in human tumors recruits and alters the function of plasmacytoid precursor dendritic cells. *Nat Med.* 2001;7(12):1339-1346.
- Bi E, et al. E-cadherin expression on multiple myeloma cells activates tumor-promoting properties in plasmacytoid DCs. *J Clin Invest.* 2018;128(11):4821-4831.
- Chauhan D, et al. Functional interaction of plasmacytoid dendritic cells with multiple myeloma cells: a therapeutic target. *Cancer Cell.* 2009;16(4):309-323.
- Munn DH, et al. Expression of indoleamine 2,3-dioxygenase by plasmacytoid dendritic cells in tumor-draining lymph nodes. *J Clin Invest.* 2004;114(2):280-290.
- Drobits B, et al. Imiquimod clears tumors in mice independent of adaptive immunity by converting pDCs into tumor-killing effector cells. *J Clin Invest.* 2012;122(2):575-585.
- Liu C, et al. Plasmacytoid dendritic cells induce NK cell-dependent, tumor antigen-specific T cell cross-priming and tumor regression in mice. *J Clin Invest.* 2008;118(3):1165-1175.
- Nierkens S, et al. Immune adjuvant efficacy of CpG oligonucleotide in cancer treatment is founded specifically upon TLR9 function in plasmacytoid dendritic cells. *Cancer Res.* 2011;71(20):6428-6437.
- Croft M, So T, Duan W, Soroosh P. The significance of OX40 and OX40L to T-cell biology and immune disease. *Immunol Rev.* 2009;229(1):173-191.
- Aspord C, Leccia MT, Charles J, Plumaz J. Plasmacytoid dendritic cells support melanoma progression by promoting Th2 and regulatory immunity through OX40L and ICOSL. *Cancer Immunol Res.* 2013;1(6):402-415.
- Lou Y, Liu C, Kim GJ, Liu YJ, Hwu P, Wang G. Plasmacytoid dendritic cells synergize with myeloid dendritic cells in the induction of antigen-specific antitumor immune responses. *J Immunol.* 2007;178(3):1534-1541.
- Pardee AD, McCurry D, Alber S, Hu P, Epstein AL, Storkus WJ. A therapeutic OX40 agonist dynamically alters dendritic, endothelial, and T cell subsets within the established tumor microenvironment. *Cancer Res.* 2010;70(22):9041-9052.
- Laplante M, Sabatini DM. mTOR signaling in growth control and disease. *Cell.* 2012;149(2):274-293.
- Sharma MD, et al. Plasmacytoid dendritic cells from mouse tumor-draining lymph nodes directly activate mature Tregs via indoleamine 2,3-dioxygenase. *J Clin Invest.* 2007;117(9):2570-2582.
- Wiley HE, Gonzalez EB, Maki W, Wu MT, Hwang ST. Expression of CC chemokine receptor-7 and regional lymph node metastasis of B16 murine melanoma. *J Natl Cancer Inst.* 2001;93(21):1638-1643.
- Chen DS, Mellman I. Oncology meets immunology: the cancer-immunity cycle. *Immunity.* 2013;39(1):1-10.
- Dalod M, et al. Dendritic cell responses to early murine cytomegalovirus infection: subset functional specialization and differential regulation by interferon α/β . *J Exp Med.* 2003;197(7):885-898.
- Le Bon A, et al. Cross-priming of CD8⁺ T cells stimulated by virus-induced type I interferon. *Nat Immunol.* 2003;4(10):1009-1015.
- Brewitz A, et al. CD8⁺ T cells orchestrate pDC-XCRI⁺ dendritic cell spatial and functional cooperativity to optimize priming. *Immunity.* 2017;46(2):205-219.
- Weinberg AD, et al. Engagement of the OX-40 receptor in vivo enhances antitumor immunity. *J Immunol.* 2000;164(4):2160-2169.
- Gough MJ, Ruby CE, Redmond WL, Dhungel B, Brown A, Weinberg AD. OX40 agonist therapy enhances CD8 infiltration and decreases immune suppression in the tumor. *Cancer Res.* 2008;68(13):5206-5215.
- Sturgis EM, Cinciripini PM. Trends in head and neck cancer incidence in relation to smoking prevalence: an emerging epidemic of human papillomavirus-associated cancers? *Cancer.* 2007;110(7):1429-1435.
- Guillaume JB, et al. Measles virus vaccine-infected tumor cells induce tumor antigen cross-presentation by human plasmacytoid dendritic cells. *Clin Cancer Res.* 2013;19(5):1147-1158.
- Cox K, et al. Plasmacytoid dendritic cells (pDC) are the major DC subset innately producing cytokines in human lymph nodes. *J Leukoc Biol.* 2005;78(5):1142-1152.
- Matsui T, et al. CD2 distinguishes two subsets of human plasmacytoid dendritic cells with distinct phenotype and functions. *J Immunol.* 2009;182(11):6815-6823.
- Zhang H, et al. A distinct subset of plasmacytoid dendritic cells induces activation and differentiation of B and T lymphocytes. *Proc Natl Acad Sci U S A.* 2017;114(8):1988-1993.
- Kumar A, et al. Enhanced oxidative phosphorylation in NKT cells is essential for their survival and function. *Proc Natl Acad Sci U S A.* 2019;116(15):7439-7448.
- Rodrigues PF, Alberti-Servera L, Eremin A, Grajales-Reyes GE, Ivanek R, Tussiwand R. Distinct progenitor lineages contribute to the heterogeneity of plasmacytoid dendritic cells. *Nat Immunol.* 2018;19(7):711-722.
- Manz MG. Plasmacytoid dendritic cells: origin matters. *Nat Immunol.* 2018;19(7):652-654.
- Dress RJ, et al. Plasmacytoid dendritic cells develop from Ly6D⁺ lymphoid progenitors distinct from the myeloid lineage. *Nat Immunol.* 2019;20(7):852-864.
- Linch SN, McNamara MJ, Redmond WL. OX40 agonists and combination immunotherapy: putting the pedal to the metal. *Front Oncol.* 2015;5:34.
- Verdeil G, Puthier D, Nguyen C, Schmitt-Verhulst AM, Auphan-Anezin N. STAT5-mediated signals sustain a TCR-initiated gene expression program toward differentiation of CD8 T cell effectors. *J Immunol.* 2006;176(8):4834-4842.
- Thiel A, Kesselring R, Pries R, Wittkopf N, Puzik A, Wollenberg B. Plasmacytoid dendritic cell subpopulations in head and neck squamous cell carcinoma. *Oncol Rep.* 2011;26(3):615-620.
- Diana J, et al. NKT cell-plasmacytoid dendritic cell cooperation via OX40 controls viral infec-

- tion in a tissue-specific manner. *Immunity*. 2009;30(2):289–299.
42. Ito T, et al. Plasmacytoid dendritic cells regulate Th cell responses through OX40 ligand and type I IFNs. *J Immunol*. 2004;172(7):4253–4259.
 43. Sawant A, et al. Depletion of plasmacytoid dendritic cells inhibits tumor growth and prevents bone metastasis of breast cancer cells. *J Immunol*. 2012;189(9):4258–4265.
 44. Le Mercier I, et al. Tumor promotion by intratumoral plasmacytoid dendritic cells is reversed by TLR7 ligand treatment. *Cancer Res*. 2013;73(15):4629–4640.
 45. Rega A, et al. Plasmacytoid dendritic cells play a key role in tumor progression in lipopolysaccharide-stimulated lung tumor-bearing mice. *J Immunol*. 2013;190(5):2391–2402.
 46. Poropatich K, et al. Comprehensive T-cell immunophenotyping and next-generation sequencing of human papillomavirus (HPV)-positive and HPV-negative head and neck squamous cell carcinomas. *J Pathol*. 2017;243(3):354–365.
 47. Riemer AB, et al. A conserved E7-derived cytotoxic T lymphocyte epitope expressed on human papillomavirus 16-transformed HLA-A2⁺ epithelial cancers. *J Biol Chem*. 2010;285(38):29608–29622.
 48. Schuler PJ, et al. EGFR-specific T cell frequencies correlate with EGFR expression in head and neck squamous cell carcinoma. *J Transl Med*. 2011;9:168.
 49. Birkeland AC, et al. Identification of targetable ERBB2 aberrations in head and neck squamous cell carcinoma. *JAMA Otolaryngol Head Neck Surg*. 2016;142(6):559–567.
 50. Pollock NI, Grandis JR. HER2 as a therapeutic target in head and neck squamous cell carcinoma. *Clin Cancer Res*. 2015;21(3):526–533.
 51. Ramos CA, et al. Human papillomavirus type 16 E6/E7-specific cytotoxic T lymphocytes for adoptive immunotherapy of HPV-associated malignancies. *J Immunother*. 2013;36(1):66–76.
 52. Carstens JL, et al. Spatial computation of intratumoral T cells correlates with survival of patients with pancreatic cancer. *Nat Commun*. 2017;8:15095.
 53. Gorris MAJ, et al. Eight-color multiplex immunohistochemistry for simultaneous detection of multiple immune checkpoint molecules within the tumor microenvironment. *J Immunol*. 2018;200(1):347–354.
 54. Johnson KS. phenoptr: inForm Helper Functions. R package version 0.1.5. <http://akoyabio.github.io/phenoptr>. Accessed April 6, 2020.
 55. Dobin A, et al. STAR: ultrafast universal RNA-seq aligner. *Bioinformatics*. 2013;29(1):15–21.
 56. Liao Y, Smyth GK, Shi W. featureCounts: an efficient general purpose program for assigning sequence reads to genomic features. *Bioinformatics*. 2014;30(7):923–930.
 57. Love MI, Huber W, Anders S. Moderated estimation of fold change and dispersion for RNA-seq data with DESeq2. *Genome Biol*. 2014;15(12):550.
 58. Robinson MD, McCarthy DJ, Smyth GK. edgeR: a Bioconductor package for differential expression analysis of digital gene expression data. *Bioinformatics*. 2010;26(1):139–140.
 59. Ritchie ME, et al. limma powers differential expression analyses for RNA-sequencing and microarray studies. *Nucleic Acids Res*. 2015;43(7):e47.
 60. Yu G, Wang LG, Han Y, He QY. clusterProfiler: an R package for comparing biological themes among gene clusters. *OMICS*. 2012;16(5):284–287.
 61. Huang DW, et al. DAVID Bioinformatics Resources: expanded annotation database and novel algorithms to better extract biology from large gene lists. *Nucleic Acids Res*. 2007;35(Web Server issue):W169–W175.
 62. Huang da W, Sherman BT, Lempicki RA. Bioinformatics enrichment tools: paths toward the comprehensive functional analysis of large gene lists. *Nucleic Acids Res*. 2009;37(1):1–13.
 63. Morgan M, Davis S. GenomicDataCommons: NIH/NCI Genomic Data Commons Access. <http://bioconductor.org/packages/GenomicDataCommons>. Accessed April 6, 2020.
 64. Morgan M, Davis S. Github. Bioconductor/GenomicDataCommons. Provide R access to the NCI Genomic Data Commons portal. <http://github.com/Bioconductor/GenomicDataCommons>. Updated January 27, 2020. Accessed April 6, 2020.
 65. Spranger S, Dai D, Horton B, Gajewski TF. Tumor-residing Batf3 dendritic cells are required for effector T cell trafficking and adoptive T cell therapy. *Cancer Cell*. 2017;31(5):711–723.e4.
 66. Chen S, et al. Host miR155 promotes tumor growth through a myeloid-derived suppressor cell-dependent mechanism. *Cancer Res*. 2015;75(3):519–531.